



● Original Contribution

CALIBRATION FOR POSITION TRACKING OF SWEEP MOTOR 3-D ULTRASOUND

JEFFREY M. ABEYSEKERA,^{*} MOHAMMAD NAJAFI,[†] ROBERT ROHLING,^{*†} and SEPTIMIU E. SALCUDEAN[†]

^{*}Department of Mechanical Engineering, University of British Columbia, Vancouver, British Columbia, Canada; and

[†]Department of Electrical and Computer Engineering, University of British Columbia, Vancouver, British Columbia, Canada

(Received 1 June 2013; revised 22 November 2013; in final form 23 November 2013)

Abstract—Tracking the position and orientation of a 3-D ultrasound transducer has many clinical applications. Tracking requires calibration to find the transformation between the tracking sensor and the ultrasound coordinates. Typically the set of image slice data are scan converted to a Cartesian volume using assumed motor geometry and a single transformation to the sensor. We propose, instead, the calibration of individual slices using a 2-D calibration technique. A best fit to a subset of slices is performed to decrease data collection time compared with that for calibration of all slices, and to reduce the influence of random errors in individual calibrations. We compare our technique with four scan conversion-based techniques: 2-D N-wire on the center slice, N-wire using a 3-D volume, N-wire using a 3-D volume including the edge points and a new closed-form planar method using a 3-D volume. The proposed multi-slice technique produced the smallest point reconstruction error (0.82 mm using a tracked stylus). (E-mail: jeffa@ece.ubc.ca) © 2014 World Federation for Ultrasound in Medicine & Biology.

Key Words: Ultrasound, Calibration, Tracking.

INTRODUCTION

Ultrasound has gained popularity because it is low cost, portable and safe and has a high frame rate. Although the majority of diagnostic ultrasound procedures use 2-D imaging, 3-D imaging can provide significant advantages (Downey et al. 2000; Nelson and Elvins 1993). For example, different 2-D imaging planes may be “re-sliced” from the 3-D ultrasound volume to provide 2-D image orientations that would be otherwise impossible to acquire, such as parallel to the skin surface. Additionally, surface or volume rendered models can be generated that may reveal pathology that is difficult to discern in conventional ultrasound images. Imaging in three dimensions can provide more information on the geometry of anatomical structures and an accurate measure of their volume. Three-dimensional ultrasound can also help in needle localization and guidance during biopsy. In this article, “2-D imaging” refers to planar images produced by transducers such as linear, curvilinear or phased arrays, and “3-D imaging” refers to ultrasound volumes produced from swept motor transducers.

Three-dimensional ultrasound data can be especially beneficial in elastography. While inducing low-frequency vibration of the tissue, 3-D ultrasound can observe the waves propagating in all three dimensions over a volume (Pospisil et al. 2010). Three-dimensional measurements can reduce overestimation of elasticity calculations by up to 60% compared with 2-D measurements (Baghani et al. 2012).

A position sensor can be attached to a swept motor transducer to allow tracking of multiple 3-D ultrasound volumes. By use of the sensor measurements, these volumes can be transformed to a global coordinate system and combined into a composite volume. Applications include intra-operative visualization (Pace et al. 2009), ablation guidance (Azizian and Patel 2011) and spatial compounding (Krücker et al. 2000), among others.

Generally, tracking systems measure the position and orientation of a sensor mounted on the ultrasound transducer with respect to a fixed base; therefore, it is necessary to calibrate the position and orientation of the image with respect to the sensor to enable these tracking techniques. Typically, this calibration is accomplished by collecting ultrasound images of objects, called *phantoms*, with known geometry and calculating the rotation and translation parameters of the calibration that best match the image features to the geometry. Phantoms are

Address correspondence to: Jeffrey M. Abeysekera, 2054-6250 Applied Science Lane, Vancouver, BC, Canada V6T 1Z4. E-mail: jeffa@ece.ubc.ca

typically constructed from spherical beads (Leotta et al. 1997), nylon wires (Prager et al. 1998) and planar surfaces (Rousseau et al. 2003).

Ultrasound calibration remains a critical factor in the overall system accuracy of ultrasound-guided procedures (Lindseth et al. 2002). The 2-D ultrasound calibration problem has been studied extensively, with reviews of many of the techniques published (Hsu et al. 2008; Mercier et al. 2005). However, it is generally not straightforward to extend 2-D calibration techniques, which make use of features in a planar image, to 3-D calibration techniques, which use volumetric structures. To be clear, we use the term *2-D calibration* to refer to the nature of the underlying data used in the calibration (i.e., a 2-D image), regardless of the transducer type. In the case of a 3-D transducer, for example, swept motor or matrix array transducers, the 2-D image used in calibration should be fixed relative to the rest of the imaging volume according to our definition. The term *3-D calibration* refers to techniques that use the entire imaging volume acquired with a 3-D transducer to extract features for calibration.

Various aspects of the 3-D ultrasound calibration problem have been investigated. One study used a 2-D calibration technique to calibrate a curvilinear transducer mounted on a motor to replicate the action of a swept motor 3-D transducer (Bouchet et al. 2001); however, in commercially available swept motor 3-D transducers, the array is enclosed in the transducer housing, so optically tracking the array location as the motor is swept is infeasible. Tracking both the transducer and phantom has shown greater accuracy compared with registering ultrasound volumes to each other, as in hand-eye techniques (Bergmeir et al. 2009). Point phantoms have been used for 3-D calibration, and are easier to use in 3-D than in 2-D because aligning the point phantom precisely with the scan plane is not as difficult with regularly spaced slices in the volume (Lang et al. 2011; Poon and Rohling 2005). For wire phantoms, the intensities of the wire reflections over the volume are iteratively matched to a reference model of the straight lines matching the phantom geometry (Bergmeir et al. 2009; Poon and Rohling 2007). A few techniques have also used planar features, and are solved by either using intensity information to iteratively match a reference, similar to the wire methods (Lange et al. 2011), or matching the zero component of the reference model of the plane to points on the plane in the volume (Baumann et al. 2006; Poon and Rohling 2007).

Typically, a swept motor transducer relies on a model of the motor geometry to calculate the location of 2-D image slices with respect to one another. Reliance on the parameters sweep angle, sweep step size and scale of the voxels and other geometry used by the ultrasound

machine to reconstruct each sweep of image slices into a Cartesian volume is considered to contribute to calibration error (Poon and Rohling 2007). This is typically not a large enough error to pose a problem with 3-D diagnostic ultrasound imaging. However, it is a problem in calibration, as each volume observing the phantom will incorrectly locate the phantom's features. It further becomes a problem after calibration when tracking the transducer, as not only are the calibration transforms incorrect, leading to placement of the volumes in the wrong position and orientation in the global coordinate system, but each volume in the collection is distorted with respect to the local transducer coordinates as well. Previous work has studied the distortions caused by errors in the sweep parameters for an untracked swept motor transducer, where highly accurate measures of organ volume were desired, and a method was presented for estimating the parameters assuming accurate alignment of the transducer with two specially designed phantoms (Tong et al. 1998).

It was the goal of the work described here to reduce errors caused by uncertainty in the motor parameters in tracked 3-D ultrasound. The intended application is the accurate measurement of tissue motion for elastography across multiple intersecting volumes (Abeysekera et al. 2012). As recent techniques developed for 2-D calibration have very high accuracy, and, assuming motor positioning is repeatable such that each image slice in a swept volume can be considered a 2-D imaging source, we proposed calibrating multiple individual 2-D image slices along the sweep, instead of scan converting the slices to a Cartesian volume and then performing a single 3-D calibration. For example, a study of a closed-form 2-D calibration using differential measurements from inclined wedges reported a point reconstruction error under 0.3 mm (Najafi et al. 2012a). Although it is difficult to compare calibration accuracy across the literature, to the best of the authors' knowledge, sub-millimeter point reconstruction accuracy has not been previously achieved in 3-D calibration techniques.

Ideally, 2-D calibration would be performed for each slice in the volume to achieve ultimate accuracy. However, because of time limitations, it is impractical to calibrate every slice. We proposed applying a best-fit path through calibration solutions calculated for a subset of the image slices along the sweep. The fit was to be used to determine the calibration transforms between the calibrated slices. The fit can also reduce the influence of error in individual calibrations, analogous to a least-squares model fitting to noisy linear data to reduce error of individual measurements.

In particular, we describe a method for fitting calibrations by separately fitting the translation and rotation parameters. The translation parameters are found by fitting an arc to the origin of each calibration. The rotation

parameters are found by solving for the best-fit geodesic on the quaternion manifold, with each calibration's rotation component representing one quaternion sample on the manifold. The fitting method described in this work is general and would function to extend any 2-D calibration technique to a 3-D swept motor transducer. In this work, we used the 2-D differential wedge technique because of its high accuracy (Najafi *et al.* 2012a). Because the technique uses multiple 2-D slices of the wedge phantom over a 3-D volume, we labeled this technique " $W_{2D \rightarrow 3D}$ ".

We evaluate the proposed multi-slice calibration approach by comparing it with several single-calibration (slice or reconstructed volume) techniques. One approach is to use a 2-D technique on a single slice in the volume, such as the well known N-wire (or Z-wire) (Comeau *et al.* 2000; Pagoulatos *et al.* 2001), and rely on the motor parameters to locate all other points in the volume relative to the calibrated slice (" N_{2D} "). Because this calibration technique ignores data at all locations along the sweep except one slice, there is potential for a lever arm effect to magnify errors when the motor is swept far from the calibrated slice. To reduce the lever arm effect, we developed a novel technique of extending the N-wire concept to reconstructed volume (3-D) by first scan converting the segmented points into a 3-D point cloud before solving for the calibration parameters (" N_{3D} "). We also present a possible improvement to the general N-wire calibration concept by solving for the outside edge points of the N-wire, in addition to the center point used in previous works (" N_{3D}^{Full} "). The N-wire technique provides the advantage of a closed-form solution compared with an iterative optimization, but has the disadvantage of providing sparse point features compared with more robustly detected planes (Prager *et al.* 1998). For a final comparison, we present a new-closed form planar-fitting calibration technique that relies on scan converted 3-D data (" P_{3D} "). Details of these methods are provided below.

METHODS

In this section we describe the calibration problem and the five techniques we used to solve it. The components and coordinate systems for the calibration are illustrated in Figure 1. The goal of calibration is to determine the fixed, rigid rotation and translation relating the image coordinate system, \mathcal{I} , and the coordinate system of the position sensor on the transducer holder, \mathcal{H} . Here the position sensor consists of markers on the holder that are tracked by a fixed optical camera system, \mathcal{O} , which also tracks markers mounted on the phantom body, \mathcal{M} . Often it is convenient to define the coordinate system of the phantom not at \mathcal{M} , but with respect to a geometrical

feature that appears in the images. This coordinate system is called \mathcal{P} , and the fixed relationship between \mathcal{P} and \mathcal{M} is determined separately *a priori* with tracked stylus measurements.

Data acquisition

All images were acquired on a SonixTouch ultrasound machine (Ultrasonix Medical, Richmond, BC, Canada), equipped with a 4DL14-5 linear array swept motor transducer, operating at a transmit frequency of 10 MHz and a depth setting of 45 mm. The transducer and phantoms were submersed in a solution of 9% by volume glycerol combined with distilled water to create a medium for the ultrasound waves to travel through at 1540 m/s to match the ultrasound machine's settings (Oates 1991).

Based on data from the manufacturer (Vernon, Tours, France), the radius of the motor is 81 mm and has an angular travel of 0.45° between slices. Both parameters were used for 3-D scan conversion. To gain complete control over the transducer's stepper motor, an intermediate circuit was constructed and placed between the transducer and the ultrasound machine. The circuit passed the ultrasound signals directly through the connectors, but provided its own stepper motor signals controlled by the parallel port on the SonixTouch.

The transducer and phantoms used for calibration had infrared, light-emitting diode (IRED) markers mounted to their bodies that were optically tracked by an Optotrak Certus motion capture system (Northern Digital, Waterloo, ON, Canada). This provided both position and orientation of coordinate systems defined using the markers on the transducer and phantom bodies with respect to the Optotrak coordinate system. To find the relationship between the IRED markers on the phantom body and the image features on the phantom, an Optotrak 4 Marker Digitizing Probe stylus with a 1.5-mm-radius ball tip was used to locate points in \mathcal{M} with known correspondence in \mathcal{P} .

The transducer was placed inside a holder that was precisely manufactured to match its outer dimensions with an Objet30 3D printer (Objet, Billerica, MA, USA) and held in place using constraining pins pushing against the top of the transducer. The IRED markers were press fit into small circular bore holes in the holder, which was reinforced with a stainless-steel frame to reduce the possibility of the holder flexing and changing the markers' positions. The holder was mounted on a goniometer, a linear translation stage and a rotary stage to allow fine adjustments of the transducer's position and orientation, before being attached to a positioning arm (Model 811-002, CIVCO Medical Solutions, Kalona, IA, USA) to fix the assembly in space. The phantoms were also attached to a positioning arm (Model 244,

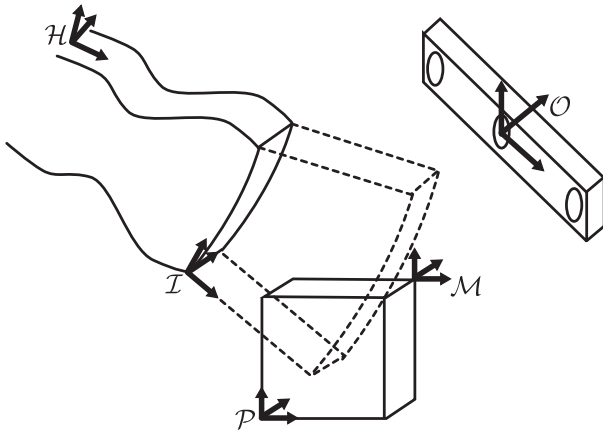


Fig. 1. Coordinate systems used in calibration procedure.

Manfrotto, Cassola, Italy) to keep the phantom fixed while recording data. The holder and one of the calibration phantoms are pictured in Figures 2 and 3.

N-wire calibration ($N2D$, $N3D$, N_{3D}^{Full})

In N-wire calibration, the geometry of the N shape is used to calculate the position of the center point, \vec{f} , based on measurements from an ultrasound image.

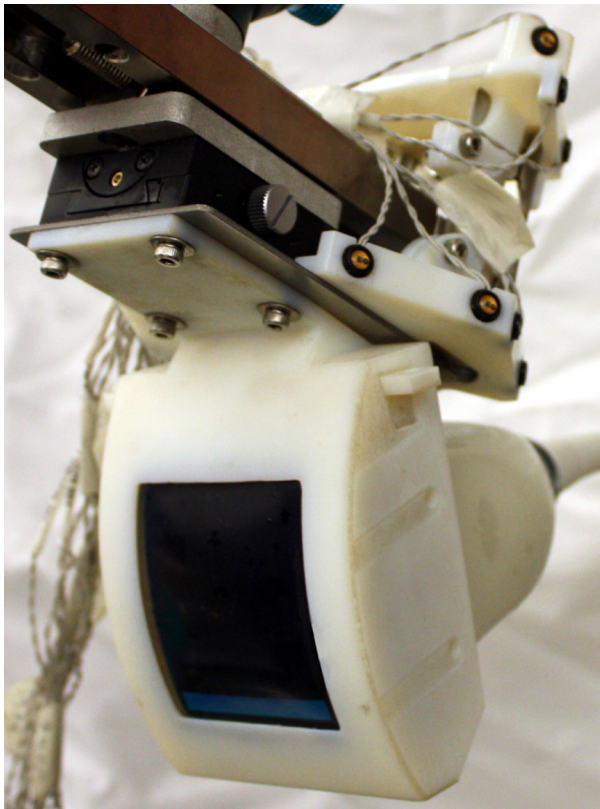


Fig. 2. Three-dimensional transducer, encased in a holder with infrared, light-emitting diode (IRED) markers.

Once at least three non-collinear center points have been found in both coordinate systems, the transform that best matches the points provides the calibration solution. Multiple center points can be obtained by acquiring an image with more than one N-wire shape visible, or acquiring additional images after transducer motion. Both techniques are used in this work to obtain an over-constrained set of points, with a phantom containing three N-wire shapes, and a collection of 10 ultrasound volumes from different positions and orientations.

The phantom was constructed with 0.3-mm nylon wire interwoven through six holes (\vec{h}_{1-6}) in an N shape, as illustrated in Figure 4. In total, the phantom contained three rows of N-wires, each spaced by 5 mm. The top-row geometry had 30 mm between \vec{h}_1 and \vec{h}_3 , 50 mm between \vec{h}_1 and \vec{h}_4 and 20 mm horizontally between \vec{h}_2 and \vec{h}_5 . The middle row had the same dimensions, but the N shape was mirrored. The bottom row had the same orientation as the top, but \vec{h}_3 , \vec{h}_5 and \vec{h}_6 were shifted 5 mm to the left. The holes were precisely located by manufacturing a rectangular block with the 3-D printer (0.028-mm resolution and 0.1-mm accuracy, as stated by the manufacturer).

The geometry of the N-wire was defined by the points \vec{a} , \vec{b} , \vec{c} and \vec{d} , which were identified in the phantom markers' coordinate system, \mathcal{M} , with a stylus and the Optotrak system. The stylus measured the hole locations, $\vec{h}_{1...6}$, and used the known geometry to find the

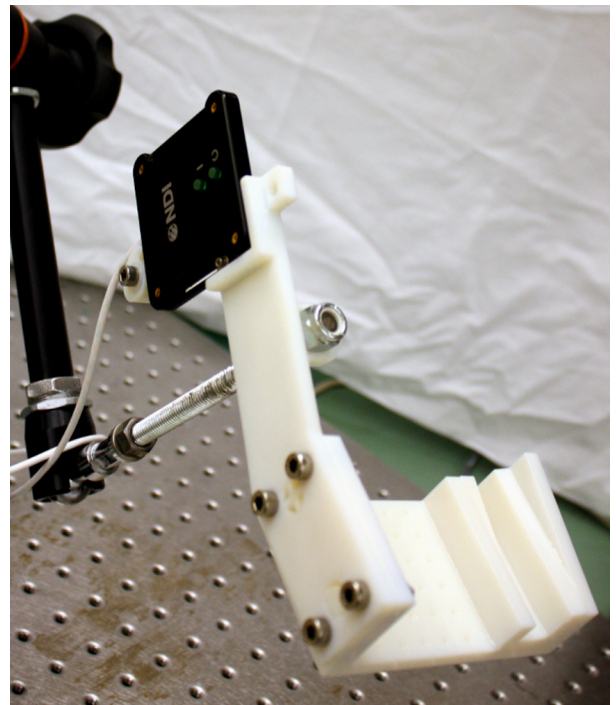


Fig. 3. Phantom used for the planar and wedge calibration methods.

corners of the N shape. The corner \vec{a} was located some scalar distance ξ along the direction $(\vec{h}_1 - \vec{h}_4)$ from the point \vec{h}_1 . The scalar distance was determined using the triangle formed by

$$\xi(\vec{h}_1 - \vec{h}_4) + \xi(\vec{h}_5 - \vec{h}_2) = \vec{h}_2 - \vec{h}_1 \quad (1)$$

The other corner points were found in a similar manner.

The nine points in each slice in the ultrasound volume were automatically segmented by performing morphological opening operations to reduce speckle and then searching for parallel lines of three collinear dots (Chen *et al.* 2009). Using the segmented points, we calculated the location of the center point in the phantom marker coordinates as

$${}^{\mathcal{M}}\vec{f} = {}^{\mathcal{M}}\vec{a} + \frac{\|{}^{\mathcal{I}}\vec{e} - {}^{\mathcal{I}}\vec{f}\|}{\|{}^{\mathcal{I}}\vec{e} - {}^{\mathcal{I}}\vec{g}\|} ({}^{\mathcal{M}}\vec{d} - {}^{\mathcal{M}}\vec{a}) \quad (2)$$

where ${}^{\mathcal{M}}\vec{f}$ and ${}^{\mathcal{I}}\vec{f}$ are located in the marker and image coordinate systems, respectively. The N_{3D} technique used all of the segmented points, whereas the N_{2D} used only the points segmented in the center slice. For each calibration technique, 10 volumes were acquired.

The collection of points described in \mathcal{M} can be transformed to \mathcal{H} using Optotrak measurements. The calibration transform can be found by matching corresponding points between \mathcal{I} and \mathcal{H} . The translation vector is the difference between the centroids of the two sets of

points, and the quaternion describing the rotation is found by solving an eigenvalue problem (Horn 1987).

The description thus far has explained only how to estimate the location of the center point along the angled segment of the N-wire, as used previously in the literature, ignoring the points on the parallel outside wires (\vec{e} and \vec{g} in Fig. 4). Including the outside points could improve the corresponding point transformation estimation. The reason that these points were ignored in previous works might be the fact that the location of the outside points in the phantom's coordinate system is not unique when based only on the lengths from the ultrasound image used to find the center point. In fact, there are two possible locations for the outside points, mirrored about a line perpendicular to outside wires and passing through the center point, as illustrated in Figures 5 and 6. Considering only one N-wire at a time, the ultrasound scan plane could pass through either the dashed line or the dash-dot line in Figure 5 and still produce the same inter-point distances in the image. However, it is possible to determine the correct line when considering all three N-wires. If we consider the three interior points in Figure 5 and all the possible exterior points (intersections of dashed and dash-dot lines with exterior wires), we obtain $2^3 = 8$ possible sets of nine points that could lie on the ultrasound plane. In general, only one of these sets lies in a plane. In Figure 6, it is clear that a plane could not pass through any set of three lines that contains any of the dash-dot lines, leaving the combination of the three dashed lines as the only possibility in this example. To select the correct set of points in this work, a plane is fitted for each case, and the plane with the smallest mean squared distance to the points is selected. The ambiguity of the transducer's position and orientation based on N-wire lengths measured in ultrasound is discussed further in Appendix A.

Planar calibration (P_{3D})

The method of planar calibration presented here is similar to a technique developed for simultaneous localization and mapping (Pathak *et al.* 2010). This technique was applied to a laser range-finding sensor, mounted on a mobile robot, which obtained a cloud of points to be segmented into planar surfaces. The planes were then matched after a change in position or orientation of the sensor to estimate the motion of the sensor. Our method does not match two sets of segmented data. Rather, it matches planes segmented in ultrasound, \mathcal{I} , to a mathematical model of the planes described in the phantom coordinate system, \mathcal{P} . Only one reconstructed ultrasound volume is required. However, collecting additional volumes after transducer motion can serve to reduce uncertainty. Our method uses a phantom designed for ultrasound calibration, where the angles for the planes

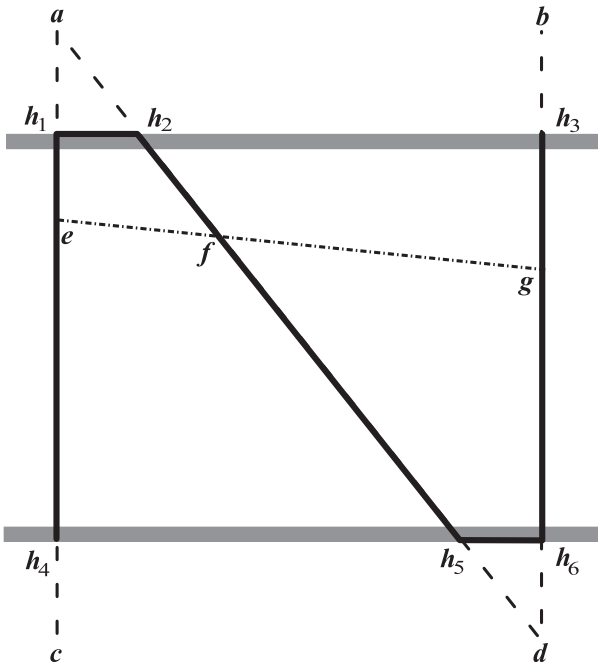


Fig. 4. Top view of one row of the N-wire phantom and the intersecting scan plane.

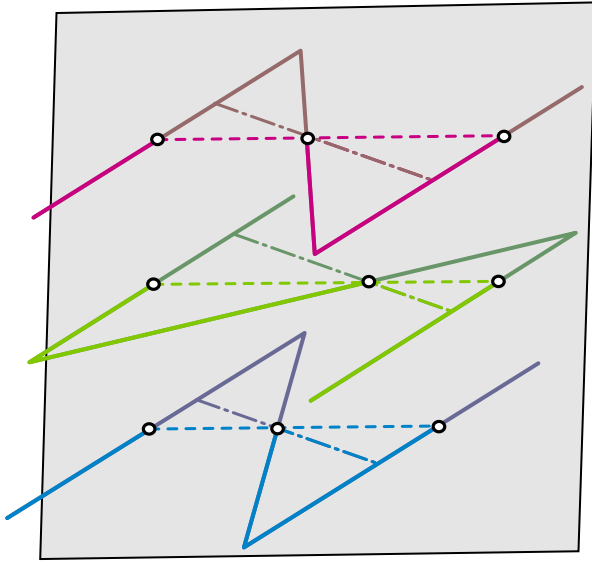


Fig. 5. Three-dimensional view of the three N-wire rows. The ultrasound scan plane, in gray, intersects each N-wire at three points, represented by the circles. A dashed line connects the intersection points in the scan plane. Based on the same interpoint distances, the lines could be mirrored to alternate orientations, represented as dash-dot lines.

were chosen to balance image quality and reliable feature extraction, while providing angles that reduce the sensitivity of the calibration to measurement errors (Najafi et al. 2012a). The calibration solution is found in two steps. First, the rotation is found by aligning the normal vectors of the planes segmented in the ultrasound volumes to the mathematical model. Next, the translation is found using the rotation solved in the first step, and by satisfying the planar equation in both the phantom and image coordinate systems.



Fig. 6. Top view of the same N-wire phantom and scanning geometry as presented in Figure 5. The N shapes are omitted in this view, but the intersection points are shown as hollow circles along the ultrasound scan plane, which is black. The dashed lines from Figure 5 all lie within the scan plane and are occluded by the black line. Considering only one N-wire row at a time, the interpoint distances could be created by the scan plane being aligned along the dash-dot line for the top (pink), middle (green) or bottom (blue) row. Noting equal depth between each dash-dot line into the page from this view, it would be impossible for the scan plane to pass through all three of the dash-dot lines, or any combination of dash-dot and dashed (occluded by the black) lines, at the same time.

Previous studies using planar features in 3-D swept ultrasound have not attempted to detect planes using 3-D data, instead using 2-D data to create clouds of points defined by maximum intensity gradients (Lange et al. 2011), Canny edge detection (Poon and Rohling 2005) and 2-D Hough transforms (Baumann et al. 2006). These studies have used iterative methods to solve the calibration problem. The technique presented here uses total least squares to find the best fit planes to 3-D data and has a closed-form solution. Based on research on 2-D calibration, both aspects tend to provide more accurate solutions (Najafi et al. 2012b; Prager et al. 1998).

The phantom was manufactured with the 3-D printer, containing five planar surfaces as pictured in Figure 3. The phantom also contains a 6×5 grid of hemispherical indents, spaced 10 mm apart in each direction, pictured in Figure 7. The location of the indents with respect to the planar surfaces is known to within the tolerance of the 3-D printer, and the radius of the hemispheres matches the radius of the stylus tip. The points are reliably located in both the phantom, \mathcal{P} , and marker, \mathcal{M} , coordinate systems with a stylus. The rigid transformation between \mathcal{P} and \mathcal{M} is determined with a corresponding point algorithm (Horn 1987).

The lines produced by the phantom surfaces are segmented in each slice in the sweep by finding the maximum intensity along each scan line. The user identifies local regions where each unique plane is located in the image. Best-fit planes are fit to the collection of maximum intensity points using principal component analysis to minimize the orthogonal distances of the points to the plane (Jolliffe 2002).

A plane can be described by the equation

$$\vec{n} \cdot \vec{x} = d \quad (3)$$

where \vec{n} is the unit normal of the plane, and d is the distance to the origin. To find the rotation from the ultrasound volume to the phantom, we maximize the dot product between the normal vectors detected from the ultrasound volume and the normal vectors of the planes known from the phantom's manufactured geometry described in the phantom coordinate system (*i.e.*, we try to make the corresponding normal vectors parallel). Using unit quaternions to represent rotation, we find the unit quaternion ${}^{\mathcal{P}}_I q$ that maximizes

$$\sum_{i=1}^k ({}^{\mathcal{P}}_I q^T n_i {}^{\mathcal{P}}_I q^*) \cdot {}^{\mathcal{P}} n_i \quad (4)$$

where ${}^I n_i$ is the i th normal vector in the ultrasound volume coordinate system, written as a purely imaginary quaternion $[0, \vec{n}_i]^T$, q^* is the conjugate of q and k is the number of planes in the volume. This equation is essentially the same as finding the rotation in the

corresponding point problem with quaternions. The difference is using normal direction vectors instead of position location vectors. The quaternion that maximizes (4) can be determined by finding the eigenvector corresponding to the maximum eigenvalue of a 4×4 symmetric matrix composed of sums of products of the elements of the normal vectors (Horn 1987).

The next step is to find the translation vector from the ultrasound volume to the phantom. Consider transforming a point from one of the planes in the ultrasound volume coordinate system to the phantom coordinate system

$${}^P\vec{p} = {}^P_R {}^I\vec{p} + {}^P\vec{t} \quad (5)$$

where P_R is the rotation found from (4), but expressed as a 3×3 rotation matrix to simplify the notation, and ${}^P\vec{t}$ is the translation that we wish to find between the two coordinate systems. Using (3), we can write

$${}^P\vec{d} = {}^P\vec{n} \bullet {}^P\vec{p} = {}^P\vec{n}^T ({}^P_R {}^I\vec{p} + {}^P\vec{t}) = ({}^P_R^T {}^P\vec{n})^T {}^I\vec{p} + {}^P\vec{n}^T {}^P\vec{t} = {}^I\vec{n}^T {}^I\vec{p} + {}^P\vec{n}^T {}^P\vec{t} = {}^I\vec{d} + {}^P\vec{n}^T {}^P\vec{t} \quad (6)$$

Given three or more planes in the ultrasound volume, we can solve for ${}^P\vec{t}$ in the least-squares sense

$${}^P\vec{t} = (A^T A)^{-1} A^T \vec{d} \quad (7)$$

where

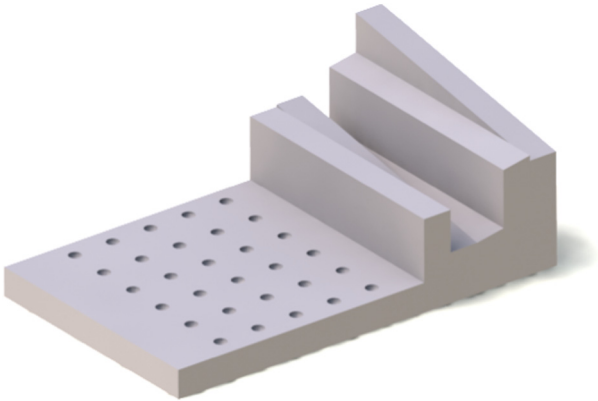


Fig. 7. Rendering of the phantom used for the planar and wedge calibration methods, excluding the infrared light-emitting diode (IRED) marker attachment. The phantom includes a grid of hemispherical indents for the stylus to measure the rigid transformation between the phantom coordinate system and the mounted IRED markers.

$$A = \begin{bmatrix} {}^P\vec{n}_1^T \\ \vdots \\ {}^P\vec{n}_k^T \end{bmatrix} \quad (8)$$

and

$$\vec{d} = \begin{bmatrix} {}^P d_1 - {}^I d_1 \\ \vdots \\ {}^P d_k - {}^I d_k \end{bmatrix} \quad (9)$$

The five planes in the phantom used in this experiment already provide redundant information with a single ultrasound volume. To match the other techniques, 10 volumes in total were acquired.

Wedge calibration on 2-D slices and then fitting ($W_{2D \rightarrow 3D}$)

The methods described thus far rely on knowing the geometry of the transducer and motor precisely to deter-

mine where each of the 2-D image slices in the ultrasound volume are located with respect to one another to scan convert the slices into a 3-D volume before identifying phantom features. We propose to perform calibration before 3-D scan conversion to reduce errors, performing 2-D calibrations at multiple slice locations and finding the best-fit path through the 2-D calibrations to link them together. Any 2-D calibration technique may be applied. We chose a recently developed, highly accurate technique, using slope measurements of wedge features from the phantom in Figure 3 (Najafi *et al.* 2012a). We perform calibrations on five slices evenly distributed across the motor sweep. The trade-off of improving the best-fit path with more calibrated slices is the time required to collect data. The 2-D wedge calibration typically requires at least 10 unique positions and orientations, with corresponding unique images, for each slice for a reliable result. Collecting data for each slice would require $10 \times 64 = 640$ unique images and poses compared with the 50 used in this work. The calibration transforms at intermediate positions are found by interpolating along the best-fit path. This method does not rely on the motor geometry; however, in-plane scan conversion is assumed to be correct (*i.e.*, the piezoelectric element spacing is known). In addition, it is assumed that the array travels along a circular arc and the relative angular positions produced by the stepper motor are accurate and repeatable. The rest of this sub-section

describes the method of interpolating between 2-D calibrations.

We consider the translation and rotation parts of the calibration interpolation separately. The translation is found using the best-fit circle to the individual translation samples from each slice calibration along the arc. In this work, circle fitting is performed using a closed-form algebraic fit, optimized to eliminate bias in the estimation (Al-Sharadqah and Chernov 2009).

The rotation is found using the best-fit geodesic on the unit quaternion manifold. The advantages of parameterizing the rotation using quaternions are that they are intuitively and compactly described by a rotation axis and angle, and it is simple to remove computational drift and restore a valid rotation through vector normalization. The quaternion manifold is a 3-sphere (S^3) sitting in 4-D space. A number of researchers have focused on the problem of interpolating rotations, where the resulting path must pass through the set of control points. Examples include spherical linear interpolation (Shoemake 1985), acceleration minimizing cubics (Park and Ravani 1997) and spherical splines (Buss and Fillmore 2001). The problem of finding a best-fit path through regression on the manifold is far less studied. One example attempts to find a geodesic on S^3 using the analogous slope and intercept for linear regression in Euclidean space with an optimization algorithm minimizing distances to the rotation samples (Fletcher 2011). The method presented here is similar; however, the mean of the rotation samples is used to locate the geodesic on the manifold, and only the direction of the geodesic is optimized instead of solving for both quantities simultaneously.

In Euclidean space, \mathbb{R}^3 , a best-fit line can be parameterized by a point on the line and a direction vector. The line passes through the centroid, or mean, of the sample points, and the sum of the orthogonal distances between the samples and the line is minimized. This line can be written as

$$\vec{x} = \vec{x}_m + t\vec{v} \quad (10)$$

where \vec{x}_m is the mean point, \vec{v} is the direction of the line and t is the scalar parameter of the line.

This same procedure can be extended to finding a best-fit geodesic on a quaternion manifold. The direction of the line in (10) can be interpreted as lying in the tangent space at the mean point. On a quaternion manifold, some mapping is required to pull the tangent back to the manifold. This is called the *exponential map*, which also has an inverse mapping from the manifold to the tangent space called the *logarithmic map*. The correspondence between the two can be seen as follows. A quaternion, q , describing a rotation around the normalized axis of

rotation, \vec{u} , by an angle, θ , can be written as (Altmann 1986)

$$\begin{aligned} q &= \cos\left(\frac{1}{2}\theta\right) + \sin\left(\frac{1}{2}\theta\right)\vec{u} \\ &= e^{\frac{1}{2}\theta\vec{u}} \end{aligned} \quad (11)$$

Taking the logarithm of (11) results in

$$\vec{v} = \frac{1}{2}\theta\vec{u} \quad (12)$$

The $+$ operator in (10) is replaced by the Lie group operator, which, for unit quaternions, is multiplication. Therefore, the best-fit geodesic on the quaternion manifold can be written using the mean quaternion, q_m , of the set of sample quaternions, and a tangent vector at the mean quaternion, \vec{v} :

$$q = q_m \exp(t\vec{v}) \quad (13)$$

The mean quaternion is found using spherical averages by first calculating a Euclidean average and projecting back to the 3-sphere, then iteratively mapping the sample points to the tangent space at the current estimate of the mean, calculating the Euclidean average in the tangent space, then mapping back to the sphere by the exponential map until the iterations converge to a single point on the sphere (Buss and Fillmore 2001).

The tangent vector at the mean quaternion, \vec{v} , is found by solving a gradient descent minimization problem, described in Appendix B. A simulation verifying the efficacy of the algorithm is provided in Appendix C.

The interpolated rotation path is bi-invariant, which means that the result is independent of the choice of coordinate system for the transducer holder (left invariance), \mathcal{H} , as well as the image slices (right invariance), \mathcal{I} . See Appendix D for a demonstration of the left and right invariance of the distance metric used for optimization. If all of the quaternion sample points were left multiplied by an arbitrary quaternion, a , then the resulting path would be

$$q = a q_m \exp(t\vec{v}) \quad (14)$$

Right multiplication of the quaternions would result in the path

$$q = q_m \exp(t\vec{v}) a \quad (15)$$

In other words, if we were to redefine the axes of any of our coordinate systems, the rotation describing the redefinition would be the same as the rotation between the original and new solution paths. This is an intuitive and desirable property, but it is not guaranteed in general for paths on the manifold. If bi-invariance was not

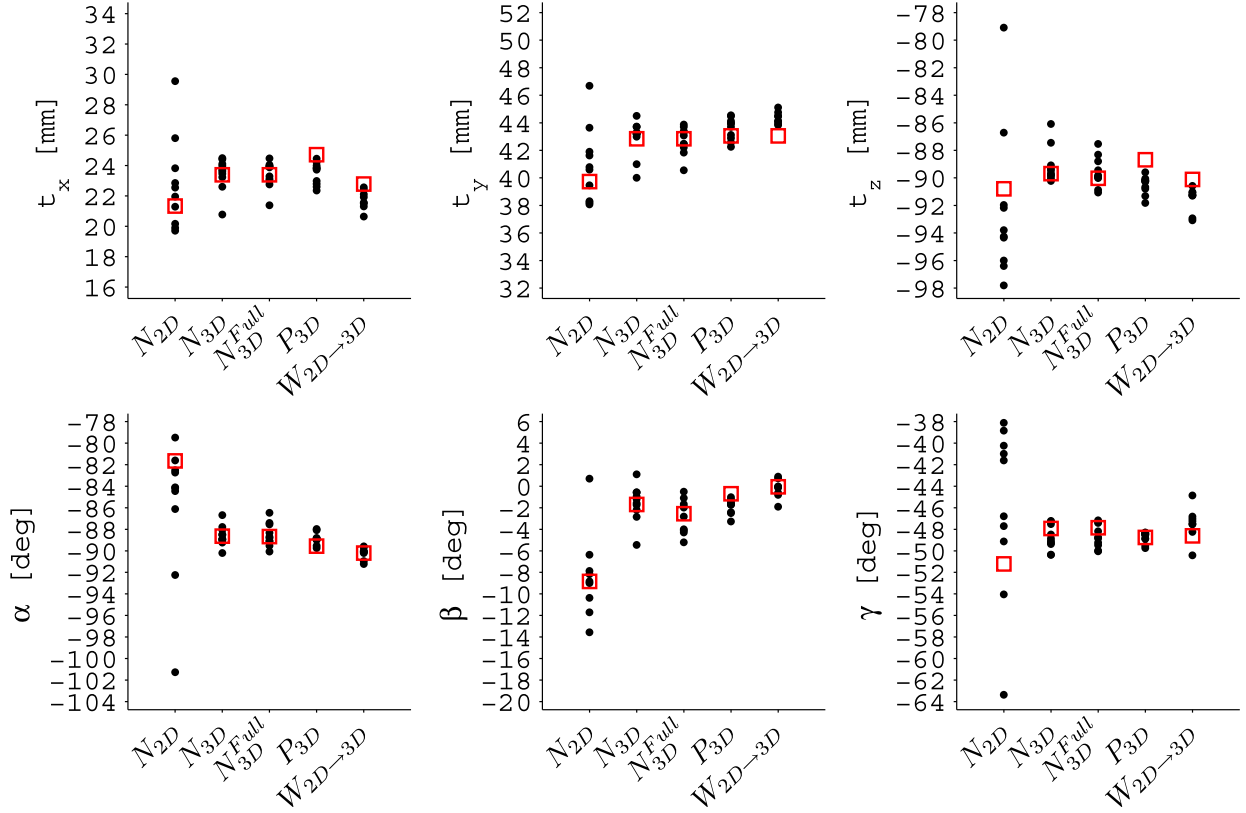


Fig. 8. Translation and rotation parameter values plotted for 10 independent tests (●), depicting the variation in the solutions. Note, N_{2D} results are converted to the same coordinates as the other methods (*i.e.*, the first slice of the sweep) using the assumed motor geometry. The parameters corresponding to a least-squares solution (□) using all of the data sets are also plotted.

satisfied, our path would depend on the definitions of the coordinate systems which can be defined arbitrarily.

Validation of the calibration methods

The calibration methods were validated by assessing repeatability and accuracy. *Repeatability* refers to how similar calibration solutions are to each other given different input data—repeating calibrations with different images should ideally still give the same transform between \mathcal{I} and \mathcal{H} because it is fixed. *Accuracy* refers to how close the calibration solution is to the true transform

between \mathcal{I} and \mathcal{H} . Because this is unknown, accuracy cannot be measured directly. Instead, accuracy is inferred by reconstructing physical quantities with known location or dimension.

To evaluate the repeatability, the standard deviation of the six degrees of freedom can be calculated after calibration with multiple independent data sets (Abeysekera and Rohling 2011; Boctor *et al.* 2004). In this work, because 10 data sets were acquired for each technique, and each technique can be solved using only one data set, the standard deviation for each technique is calculated for 10 independent trials. In the case of W_{2D}→3D, the standard deviation is calculated after applying fits to 10 randomly selected unique combinations of the 10 calibrations at each of the five calibration locations.

Two point reconstruction tests were used to evaluate the calibration accuracy. Point reconstruction tests calculate the difference between points with known locations and segmented points transformed to the same coordinate system using a calibration solution. In both of the tests, all 10 data sets were used to solve for a single least squares solution for each method.

Table 1. Standard deviation of the three translation DOF and three rotation DOF after 10 trials using a single data set for calibration

	N2D	N3D	N _{3D} ^{Full}	P _{3D}	W _{2D} →3D
t_x (mm)	3.05	1.09	0.89	0.73	0.63
t_y (mm)	2.72	1.35	1.00	0.80	0.44
t_z (mm)	5.55	1.31	1.09	0.66	0.92
α (°)	6.38	0.94	1.09	0.55	0.58
β (°)	7.13	1.73	1.57	0.68	0.89
γ (°)	7.96	1.16	1.08	0.51	1.54

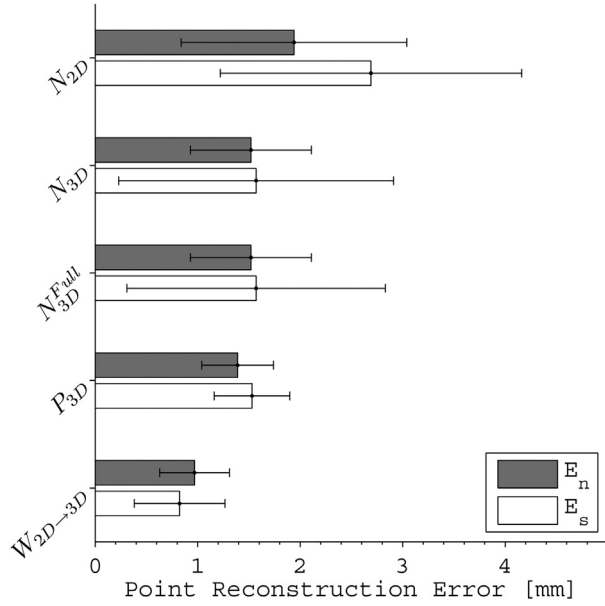


Fig. 9. Point reconstruction error for the calibration techniques, using the N-wire phantom as validation (E_n) and the stylus (E_s). The bars indicate the means, and the error bands indicate the standard deviations.

The first point reconstruction test used a tracked stylus as the object to be imaged (Poon and Rohling 2007). The stylus and transducer were both moved between each of 25 volume acquisitions. The ball tip was manually segmented by finding the slice in each volume with the strongest comet-tail reverberation, centering a line along the reverberation, and selecting the top of the bright intensity response of the tip (Adebar et al. 2012). The bright response corresponds to the top of the sphere (Hacihaliloglu et al. 2009); the center of the sphere was estimated by adding a distance equal to the radius along the direction of the scan line. The point reconstruction error is calculated between the stylus tip, as measured by the Optotrak system, and the tip segmented in the images and then transformed into the Optotrak coordinates using the calibration solution

$$E_s(v) = \|\mathcal{O}\vec{x} - \mathcal{O}_{\mathcal{H}}T_{v\mathcal{I}}^{\mathcal{H}}T^{\mathcal{I}}\vec{x}\| \quad (16)$$

where \vec{x} is the stylus tip, T describes the rigid transformation operation and error is calculated for the v th volume acquired of the stylus tip.

The second point reconstruction test used the N-wire phantom (Najafi et al. 2012a). A single volume of the phantom was acquired, distinct from the 10 used in the N-wire calibrations. Only the center points of each N shape were used for evaluation with a total of 78 center points segmented in the volume. The center points are

known in \mathcal{M} from geometry as described under Methods. These points can be transformed to \mathcal{H} using the Optotrak measurements. The same center points in \mathcal{I} can be transformed to \mathcal{H} using the calibration solution. The error is the magnitude of the difference between these two sets of points

$$E_n(i, v) = \|\mathcal{O}_{\mathcal{H}}T_v^{-1}\mathcal{O}_{\mathcal{M}}T_v^{\mathcal{M}}\vec{x}_i - \mathcal{O}_{\mathcal{H}}T^{\mathcal{I}}\vec{x}_i\| \quad (17)$$

where the error is calculated for $i \in [1 \dots 3]$ center points in each volume.

RESULTS

The calibration results from each of the 10 data sets for all of the calibration methods are plotted in Figure 8. The results are separated into six degrees of freedom (DOF): translation from the image to the holder (t_x , t_y , t_z) and Euler angles defined using the fixed image coordinate axes and applying first a rotation by γ around the x -axis, followed by a rotation by β around the y -axis and finally a rotation by α around the z -axis. It should be noted that these results cannot be used to assess the accuracy of the calibration methods, as the true calibration solution is unknown; however, it does provide a measure of the calibration repeatability. A calibration method is more repeatable when the solutions are more closely spaced. On the basis of Figure 8, the most repeatable methods are P_{3D} and W_{2D}→_{3D}. This is quantified later in the Results section using standard deviation. The least-squares solution using all of the 10 data sets for each calibration method is also plotted. Although a few points appear to be outliers, the outliers do not correspond to each other across the six DOF (e.g., an outlier in t_x does not correspond to an outlier in t_y). The least-squares solution is clearly not a mean of the individual solutions in each DOF, and does not necessarily even lie within the spread of the individual solutions in each DOF, because the least-squares solution fits all six degrees of freedom at once.

The standard deviations of the six DOF for each of the calibration techniques are listed in Table 1. A smaller standard deviation indicates that the solutions are repeatable with a different input of transducer positions and orientations and corresponding images. This is desirable as it indicates that the method is not sensitive to the exact motion of the transducer used to collect the images, as well as the image quality. The most repeatable calibration based on the standard deviation results is W_{2D}→_{3D} for t_x and t_y and P_{3D} for the remaining DOF.

The mean and standard deviation of the point reconstruction error as calculated using both the N-wire phantom and stylus tip as validation tools are illustrated in

Figure 9. These results serve as an indirect measure of calibration accuracy. Based on the mean error, $W_{2D \rightarrow 3D}$ is the most accurate technique in both the E_n and E_s tests ($p < 0.01$). All of the techniques are significantly more accurate than N_{2D} .

DISCUSSION

The stylus used in this study served two purposes: to measure the coordinate systems for the phantoms, and to provide points measured in the tracker's coordinate system for validation in the point reconstruction test. To understand how the stylus contributed to the errors in this study, we can study how well the stylus measures known distances, as well as how much the stylus location varies at a measurement point. The columns of the stylus grid on the slope phantom are 50 mm in total length. Averaging over the five columns, the mean and standard deviation of the absolute error in the distance measurement using the stylus were 0.02 and 0.03 mm, respectively. To measure how much the stylus location varies, the standard deviations of stylus location at the 30 grid points were averaged, resulting in a value of 0.11 mm. These results suggest stylus error has little effect on calibration or the point reconstruction test.

Comparison of the performance of the calibration methods studied in the work described here with previous results produced by other research groups should be done with caution because of differences in materials, equipment and acquisition protocol. In addition, not all methods in the literature evaluate the calibrations using the same definitions of point reconstruction error. One study matched five tracked ultrasound volumes to a model of a phantom containing two egg-shaped 3-D features to calibrate, and simulation of optical tracking errors found a mean point reconstruction error of 2.0 mm (Lange and Eulenstein 2002). A study using only a single volume and four point fiducials for calibration measured root mean square (RMS) point reconstruction errors of 5.1 and 5.5 mm, over two cross-wire point measurements repeated 10 times each and located in tracker coordinates using a stylus (Poon and Rohling 2007). A study comparing three calibration methods (IXI-wire, cube and stylus) found RMS point reconstruction errors over 10 stylus validation points of 2.15, 4.91 and 2.36 mm, using one, one and five tracked ultrasound volumes, respectively (Poon and Rohling 2005). Another study comparing separable and combined hand-eye calibrations (the phantom is not tracked), as well as a tracked phantom approach, all with a cross-wire phantom, calculated error between points sets generated over a 50^3-mm^3 volume spaced by 5 mm in each direction, and found mean errors of 5.9, 3.5 and 3.3 mm, respectively (Bergmeir *et al.* 2009). To the best of our knowledge, $W_{2D \rightarrow 3D}$ is the first

3-D ultrasound calibration to demonstrate potential for sub-millimeter point reconstruction accuracy with a mean of 0.82 mm with the stylus validation and 0.97 mm with the N-wire validation. To compare with the results in the literature reported as RMS values, the RMS error for the $W_{2D \rightarrow 3D}$ method with the stylus validation was 0.93 mm, and that with the N-wire validation was 1.03 mm.

Including the outside points for the full N-wire calibration (N_{3D}^{Full}) did not provide a significant improvement in accuracy compared with the traditional center point N-wire calibration (N_{3D}). However, (N_{3D}^{Full}) did provide a small improvement in repeatability. It is important to remember that these results used multiple volumetric sweeps over the phantom, resulting in thousands of corresponding points used for calibration. In cases where the number of points may be more limited, for example in the case of 2-D calibration, the full N-wire technique may prove to be of greater practical significance. Using a single 2-D image for calibration, including the outside points, reduced the standard deviations of the six DOF ($t_x, t_y, t_z, \alpha, \beta, \gamma$) over 10 independent trials by 29%, 11%, 10%, 28%, 8% and 22%, respectively.

The N-wire configuration used in this experiment enabled unique determination of the edge points for (N_{3D}^{Full}). The edge points cannot be determined for all possible N-wire configurations. For example, using only two rows of the configuration presented in this article allows the possibility of the plane tilting to pass through two of the alternate lines in Figure 6. However, finding the common plane to the three-row configuration presented in this article is not the only method of determining the edge points. One possible alternative is to place two N-wires side-by-side. In this configuration, the alternate line for one of the N-wires would produce incorrect interpoint distances in the second N-wire. The trade-off for the side-by-side configuration is a lower sensitivity because of a shallower angle for the diagonal segments to fit the width of the image.

CONCLUSIONS

The process of scan conversion to convert swept ultrasound data into a Cartesian volume relies on estimates of motor parameters which can introduce errors into the calibration process. To overcome the reliance on motor parameters, we proposed performing multiple 2-D calibrations and finding a best-fit path through them ($W_{2D \rightarrow 3D}$). The proposed method can be applied to any 2-D calibration technique; however, we chose a wedge phantom because of its high accuracy in two dimensions. We developed four techniques to compare against the fitting method. Three were based on extending the 2-D N-wire calibration technique into three dimensions. The

fourth (P_{3D}) used planar features for calibration, and is the first planar technique to have a closed-form solution for 3-D swept ultrasound.

The repeatability of the calibrations was evaluated using the standard deviations of the six DOF after multiple trials on independent input data, and P_{3D} was found to be the most repeatable. Overall accuracy was evaluated using two point reconstruction tests and $W_{2D \rightarrow 3D}$ had the highest accuracy in both tests. The accuracy and repeatability of the N-wire phantom methods were improved by using 3-D data compared with sweeping from a 2-D calibration.

The fitted calibration approach, $W_{2D \rightarrow 3D}$, was able to achieve sub-millimeter accuracy. On the basis of previous work, sub-millimeter tracking accuracy is required in elastography applications to realize the benefits of multiple ultrasound views for tissue motion measurements compared with beam steering methods (Abeysekera et al. 2012). This should enable use of tracked swept motor ultrasound in elastography to improve 3-D tissue motion estimates. Future work will investigate the benefits of using tracked 3-D ultrasound to measure tissue motion and calculate elasticity. In applications where ease of use is paramount, while still retaining a high accuracy and repeatability, P_{3D} offers the best compromise.

Acknowledgments—This work is supported by the Natural Sciences and Engineering Research Council of Canada and the Canadian Institutes of Health Research.

REFERENCES

- Abeysekera JM, Rohling R. Alignment and calibration of dual ultrasound transducers using a wedge phantom. *Ultrasound Med Biol* 2011;37:271–279.
- Abeysekera JM, Zahiri-Azar R, Goksel O, Rohling R, Salcudean SE. Analysis of 2-D motion tracking in ultrasound with dual transducers. *Ultrasonics* 2012;52:156–168.
- Adebar TK, Yip MC, Salcudean SE, Rohling RN, Ngan CY, Goldenberg SL. Registration of 3D ultrasound through an air-tissue boundary. *IEEE Trans Med Imaging* 2012;31:2133–2142.
- Akaike H. A new look at the statistical model identification. *IEEE Trans Autom Control* 1974;19:716–723.
- Al-Sharadqah A, Chernov N. Error analysis for circle fitting algorithms. *Electronic J Statist* 2009;3:886–911.
- Altmann SL. Rotations, quaternions, and double groups. New York: Oxford University Press (Clarendon); 1986.
- Azizian M, Patel R. Intraoperative 3D stereo visualization for image-guided cardiac ablation. *Proc SPIE Vol* 2011;7964:79640F.
- Baghani A, Eskandari H, Wang W, Da Costa D, Lathiff M, Sahebjavaher R, Salcudean S, Rohling R. Real-time quantitative elasticity imaging of deep tissue using free-hand conventional ultrasound. In: Proceedings, MICCAI 2012: Medical Image Computing and Computer-Assisted Intervention. Lecture Notes Comput Sci 2012;7511:617–624.
- Baumann M, Daanen V, Leroy A, Troccaz J. 3-D ultrasound probe calibration for computer-guided diagnosis and therapy. *Comput Vision Approaches Med Image Anal* 2006;4241:248–259.
- Bergmeir C, Seitel M, Frank C, Simone RD, Meinzer HP, Wolf I. Comparing calibration approaches for 3D ultrasound probes. *Int J Comput Assist Radiol Surg* 2009;4:203–213.
- Boctor E, Viswanathan A, Choti M, Taylor RH, Fichtinger G, Hager G. A novel closed form solution for ultrasound calibration. In: Proceedings, IEEE International Symposium on Biomedical Imaging: Nano to Macro, Arlington, Virginia, USA, 15–18 April 2004. Vol. 1. New York: IEEE, 2004:527–530.
- Bouchet LG, Meeks SL, Goodchild G, Bova FJ, Buatti JM, Friedman WA. Calibration of three-dimensional ultrasound images for image-guided radiation therapy. *Phys Med Biol* 2001;46:559–577.
- Buss SR, Fillmore JP. Spherical averages and applications to spherical splines and interpolation. *ACM Trans Graphics* 2001;20:95–126.
- Chen TK, Thurston AD, Ellis RE, Abolmaesumi P. A real-time freehand ultrasound calibration system with automatic accuracy feedback and control. *Ultrasound Med Biol* 2009;35:79–93.
- Comeau RM, Sadikot AF, Fenster A, Peters TM. Intraoperative ultrasound for guidance and tissue shift correction in image-guided neurosurgery. *Med Phys* 2000;27:787–800.
- Downey DB, Fenster A, Williams JC. Clinical utility of three-dimensional US. *Radiographics* 2000;20:559–571.
- Fletcher PT. Geodesic regression on Riemannian manifolds. In: Proceedings, Third International Workshop on Mathematical Foundations of Computational Anatomy—Geometrical and Statistical Methods for Modelling Biological Shape Variability, 2011:75–86.
- Hacihaliloglu I, Abugharbieh R, Hodgson AJ, Rohling RN. Bone surface localization in ultrasound using image phase-based features. *Ultrasound Med Biol* 2009;35:1475–1487.
- Horn BKP. Closed-form solution of absolute orientation using unit quaternions. *J Opt Soc Am A* 1987;4:629–642.
- Hsu PW, Prager RW, Gee AH, Treece GM. Freehand 3D ultrasound calibration: a review. In: Sensen CW, Hallgrímsson B, (eds). *Advanced imaging in biology and medicine*. Berlin: Springer-Verlag; 2008. p. 47–84.
- Jolliffe IT. Principal component analysis. 2nd ed. New York: Springer-Verlag; 2002.
- Krucker JF, Meyer CR, LeCarpentier GL, Fowlkes JB, Carson PL. 3D spatial compounding of ultrasound images using image-based nonrigid registration. *Ultrasound Med Biol* 2000;26:1475–1488.
- Lang A, Parthasarathy V, Jain A. Calibration of 3D ultrasound to an electromagnetic tracking system. *Proc SPIE* 2011;7968:79680W.
- Lange T, Eulenstein S. Calibration of swept-volume 3-D ultrasound. In: Proceedings, 6th Annual Conference on Medical Image Understanding and Analysis. Vol. 99. 2002:29–32.
- Lange T, Kraft S, Eulenstein S, Lamecker H, Schlag PM. Automatic calibration of 3D ultrasound probes. In: Proceedings, Bildverarbeitung für die Medizin, 2011:169–173.
- Leotta DF, Detmer PR, Martin RW. Performance of a miniature magnetic position sensor for three-dimensional ultrasound imaging. *Ultrasound Med Biol* 1997;23:597–609.
- Lindseth F, Langø T, Bang J, Hernes TAN. Accuracy evaluation of a 3D ultrasound-based neuronavigation system. *Comput Aided Surg* 2002;7:197–222.
- Mercier L, Langø T, Lindseth F, Collins LD. A review of calibration techniques for freehand 3-D ultrasound systems. *Ultrasound Med Biol* 2005;31:449–471.
- Najafi M, Afsham N, Abolmaesumi P, Rohling R. A closed-form differential formulation for ultrasound spatial calibration. In: Information Processing in Computer-Assisted Interventions. Lecture Notes Comput Sci 2012a;7330:44–53.
- Najafi M, Afsham N, Abolmaesumi P, Rohling R. Single wall closed-form differential ultrasound calibration. *Proc SPIE* 2012b;8316:83162A.
- Nelson TR, Elvins TT. Visualization of 3D ultrasound data. *IEEE Comput Graphics Appl* 1993;136:50–57.
- Oates CP. Towards an ideal blood analogue for Doppler ultrasound phantoms. *Phys Med Biol* 1991;36:1433–1442.
- Pace DF, Wiles AD, Moore J, Wedlake C, Gobbi DG, Peters TM. Validation of four-dimensional ultrasound for targeting in minimally-invasive beating-heart surgery. *Proc SPIE* 2009;7261:726115.
- Pagoulatos N, Haynor DR, Kim Y. A fast calibration method for 3-D tracking of ultrasound images using a spatial localizer. *Ultrasound Med Biol* 2001;27:1219–1229.

- Park FC, Ravani B. Smooth invariant interpolation of rotations. *ACM Trans Graphics* 1997;16:277–295.
- Pathak K, Birk A, Vaškevičius N, Poppinga J. Fast registration based on noisy planes with unknown correspondences for 3-D mapping. *IEEE Trans Robotics* 2010;26:424–441.
- Poon TC, Rohling RN. Comparison of calibration methods for spatial tracking of a 3-D ultrasound probe. *Ultrasound Med Biol* 2005;31:1095–1108.
- Poon TC, Rohling RN. Tracking a 3-D ultrasound probe with constantly visible fiducials. *Ultrasound Med Biol* 2007;33:152–157.
- Pospisil ER, Rohling R, Zahiri-Azar R, Salcudean SE. 4-D \times 3-D ultrasound: Real-time scan conversion, filtering, and display of displacement vectors with a motorized curvilinear transducer. *IEEE Trans Ultrason Ferroelectr Freq Control* 2010;57:2271–2283.
- Prager RW, Rohling RN, Gee AH, Berman L. Rapid calibration for 3-D freehand ultrasound. *Ultrasound Med Biol* 1998;24:855–869.
- Rousseau F, Hellier P, Barillot C. Robust and automatic calibration method for 3D freehand ultrasound. In: *Proceedings, MICCAI 2003: Medical Image Computing and Computer-Assisted Intervention. Lecture Notes Comput Sci* 2003;2879:440–448.
- Shoemake K. Animating rotation with quaternion curves. In: *SIGGRAPH '85: Proceedings, 12th Annual Conference on Computer Graphics and Interactive Techniques*. New York: ACM, 1985:245–254.

- Tong S, Cardinal HN, Downey DB, Fenster A. Analysis of linear, area and volume distortion in 3-D ultrasound imaging. *Ultrasound Med Biol* 1998;24:355–373.

APPENDIX A

This appendix illustrates the ambiguity in the transducer orientation based on interpoint distance measures of N-wire features in ultrasound images. The ambiguity makes it difficult to determine the location of the outside edge points of the N-wire in phantom coordinates. One possible solution was presented in the Methods section. The phantom geometry used in the article is considered in this appendix while considering different numbers and combinations of N-wires. The figures illustrate renderings of a L14-5/38 linear array to simplify the understanding of each of the slices obtained from the motorized 4DL14-5/38 transducer.

The phantom contains three rows of N-wires as described under Methods. The interpoint distances (left/right) from the top N-wire to the bottom are 15/20, 21.6/13.4 and 13.1/16.1 mm, matching the distances in Figure 5.

First, we can consider only one N-wire at a time. If we use the distances measured in the ultrasound image, we can look at the N-wire model and draw a line across the N-wire, where the angled wire cuts the line into two segments with lengths matching the measurements. There are two possible lines that can satisfy the measurements. The two lines for each of the three N-wires are illustrated in Figure 10. In

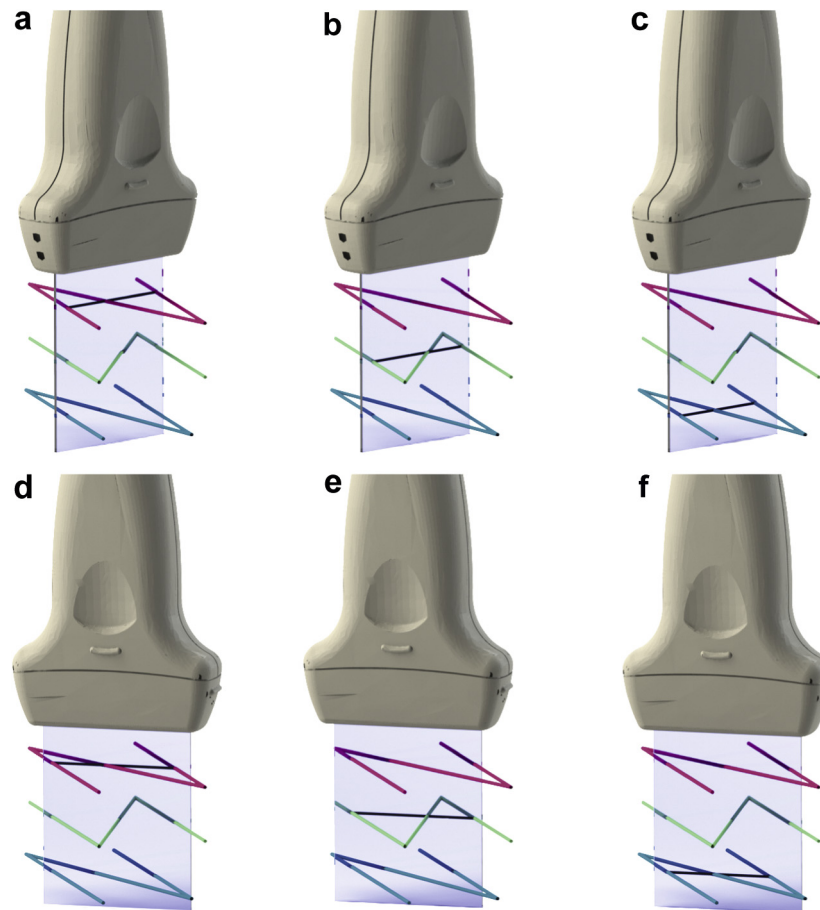


Fig. 10. By observation of the interpoint distances for one N-wire at a time, the transducer orientation can be constrained to rotate about an axis. The interpoint distances allow for two possible axes for each N-wire. For simplicity, the transducer is shown only orthogonal to the plane of the N-wire. The first set of possible axes (black) for the (a) top, (b) middle and (c) bottom N-wires, and the second set of axes for the (d) top, (e) middle and (f) bottom.

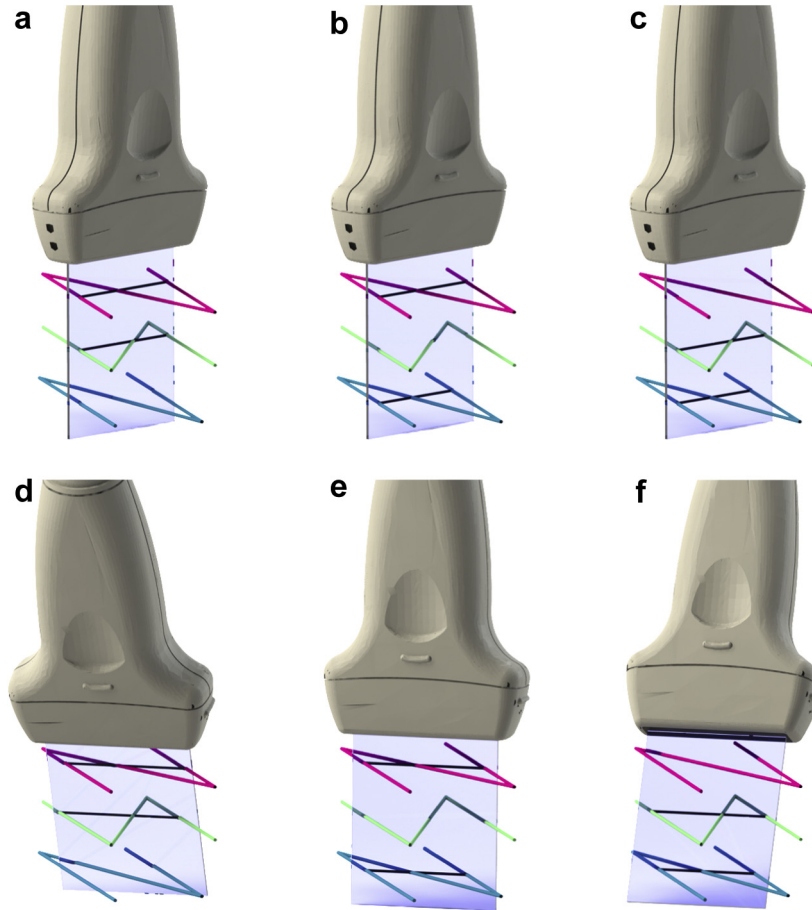


Fig. 11. By observation of the interpoint distances for two N-wires at a time, the transducer orientation can be fully constrained. Using the first set of possible axes (black) from the first row of Figure 10, the image plane can pass through the axes for the (a) top and middle, (b) top and bottom, or (c) middle and bottom N-wires. Similarly, using the second set of possible axes from the second row of Figure 10, the image plane can be fit to the axes for the (d) top and middle, (e) top and bottom, or (f) middle and bottom N-wires. It is impossible for the plane to pass through a combination of one of the first possible axes and one of the second possible axes, thus there are six possible positions and orientations for the image plane when considering the interpoint distances for two N-wires.

Figure 10(a–c), the transducer is in the same position and orientation. This happens to be the position and orientation that satisfy the interpoint distances for all three N-wires simultaneously. In Figure 10(d–f), the transducer translates slightly between N-wire choices, and is rotated compared with Figure 10(a–c). It should be noted that the transducer in Figure 10 can be rotated about a line's axis and still satisfy the measurements. The transducer is shown only orthogonal to the plane of the N-wires for simplicity. It is clear that because there are multiple transducer positions and orientations that satisfy the measurements, the outside edge points cannot be determined.

It is also illustrative to consider more than one N-wire at a time. If two N-wires are considered, then there are 12 possible combinations of the axes from Figure 10: three choices in N-wires, and two possible axes for each N-wire ($3 \times 2 \times 2 = 12$). However, only 6 combinations are coplanar. The non-planar combinations are not physically realizable because the image is planar. In Figure 11(a–c), the transducer is again in the same position and orientation throughout, which are the correct position and orientation to satisfy all three N-wires simultaneously. In Figure 11(d–f), the transducer clearly needs to change its position and orientation to fit the different combinations of two N-wires and would not satisfy all three simultaneously.

Finally, considering all three rows of N-wires at the same time results in only one possible combination that remains coplanar. The solution is illustrated in Figure 12. Now that the position and orientation are uniquely defined, the outside edge points can be located in the phantom coordinates and included in the corresponding point algorithm for calibration.

APPENDIX B

This appendix describes the method for solving for the tangent vector that defines the direction of the best-fit geodesic on the quaternion manifold for the $W_{2D \rightarrow 3D}$ calibration method. The tangent vector is found using a gradient descent algorithm. The initial guess is the tangent vector from the mean quaternion to the last quaternion in the set:

$$\vec{v} = \log(q_m^* q_N) \quad (18)$$

The objective is to minimize the sum of the geodesic distances between the quaternion sample points and the best-fit geodesic. However, because the sample points are all located near the mean, the geodesic

distance can be approximated in the tangent space. The quaternions are mapped to the tangent space at q_m :

$$\vec{p}_i = \log (q_m^* q_i) \quad (19)$$

Now we need to minimize the sum of the orthogonal distances between the \vec{p}_i and the line described by \vec{v} . The squared distance can be computed using

$$\begin{aligned} d_i^2 &= \frac{\|\vec{v} \times \vec{p}_i\|^2}{\|\vec{v}\|^2} \\ &= \frac{\|[\vec{p}_i]_{\times}^T \vec{v}\|^2}{\|\vec{v}\|^2} \end{aligned} \quad (20)$$

where \times represents the cross-product operator, and $[\cdot]_{\times}$ is a skew symmetric matrix. To minimize the distances, we require the gradient of (20). If we let $h = \|[\vec{p}_i]_{\times}^T \vec{v}\|^2$, and $g = \|\vec{v}\|^2$, then the familiar quotient rule results in

$$\frac{(d_i^2)}{\vec{v}} = \frac{h}{g} \frac{g - \frac{g}{g} h}{g^2} \quad (21)$$

The derivatives of h and g are given by

$$\frac{h}{\vec{v}} = 2[\vec{p}_i]_{\times} [\vec{p}_i]_{\times}^T \vec{v} \quad (22)$$

and

$$\frac{g}{\vec{v}} = 2 \vec{v} \quad (23)$$

It would be convenient to parameterize the geodesic in (13) such that the scalar parameter $t \in [0, 1]$, with 0 corresponding to the start of the geodesic path, 0.5 at the mean quaternion and 1 at the end of the path. However, \vec{v} is arbitrarily scaled and is located at q_m . We can instead define a new scalar parameter, s , as a function of t , which uses the projections of the first and last quaternions mapped to the tangent space onto \vec{v}

$$s(t) = a + t(b-a) \quad (24)$$

where

$$a = \frac{\vec{p}_1 \cdot \vec{v}}{\|\vec{p}_1\| \|\vec{v}\|} \quad (25)$$

and

$$b = \frac{\vec{p}_N \cdot \vec{v}}{\|\vec{p}_N\| \|\vec{v}\|} \quad (26)$$

Now the best-fit geodesic can be described by

$$q = q_m \exp (s \vec{v}) \quad (27)$$

APPENDIX C

A simulation was used to evaluate the rotation fitting algorithm for the $W_{2D \rightarrow 3D}$ calibration interpolation. A set of $n = 8$ quaternions was generated, evenly spaced along a geodesic, starting at the identity rotation, $q_1 = [1, 0, 0, 0]^T$, and following a rotation about the z -axis, $\vec{w} = [0, 0, \pi/4]^T$. Error for each quaternion was simulated with an isotropic Gaussian distribution, with standard deviation σ , in the tangent space, $\vec{\epsilon}$. Thus, each noisy quaternion is described by

$$q_i = q_1 \exp (t_i \vec{w}) \exp (\vec{\epsilon}) \quad (28)$$

where $i \in [1 \dots n]$, and

$$t_i = \frac{i-1}{n-1} \quad (29)$$

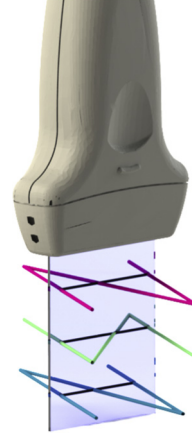


Fig. 12. Observing the interpoint distances for all three N-wires at the same time allows for only one co-planar solution.

To evaluate the performance of the fit, an error metric was defined as the geodesic distance between the last quaternion in the simulated set and the same quaternion using the best-fit geodesic:

$$E = \|\log ((q_1 \exp (\vec{w}))^* (q_m \exp (\vec{v})))\| \quad (30)$$

The simulation was run for three different values of σ : $\pi/32$, $\pi/16$ and $\pi/8$. As σ is increased, it is expected that the mean and standard deviation of E should also increase. The log-normal distribution of E provided the best statistical model fit (based on the minimum information theoretical criterion estimate [Akaike 1974]). The mean and standard deviation of E after 1000 simulations for the three different levels of σ are illustrated

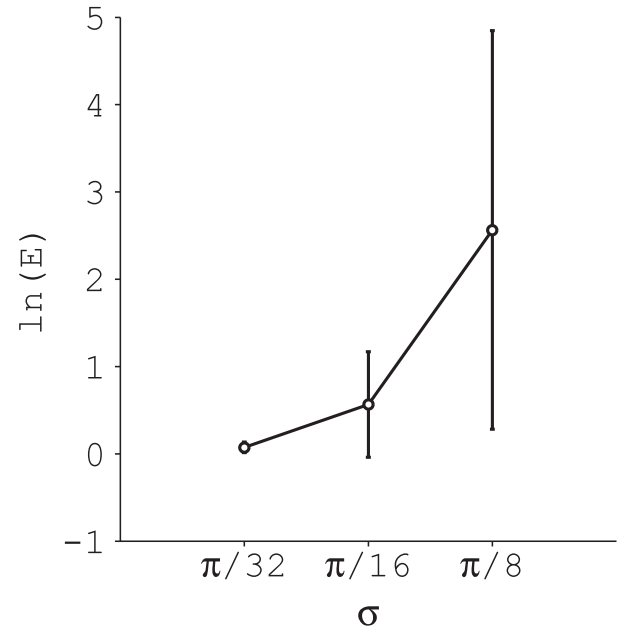


Fig. 13. Plot of the mean and standard deviation of the best-fit geodesic error metric after taking the natural logarithm of the set to transform the distribution closer to normal. The values are plotted for three different levels of simulated Gaussian noise, with standard deviation σ , on the eight quaternions used for fitting after 1000 simulation trials for each noise level.

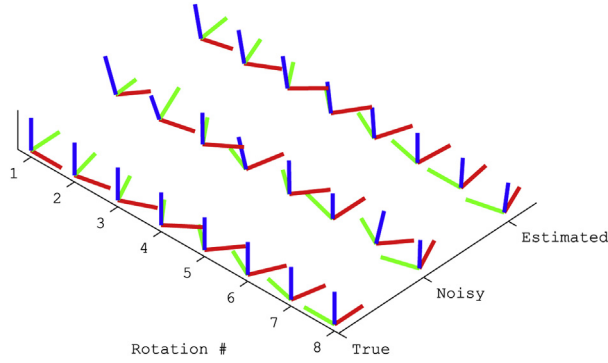


Fig. 14. Visual depiction of fitting the rotation samples with axes indicating the rotation orientation. The true rotations are equally sampled along a 90° rotation about the z -axis. The noisy rotations have isotropic Gaussian noise ($\sigma = \pi/16$) applied to each sample. After fitting the best-fit geodesic curve to the noisy samples, eight equally spaced rotations are interpolated from the curve to provide the estimated rotations.

in Figure 13. To visualize the effectiveness of the proposed fitting method in the presence of noise, axes indicating orientation defined by each quaternion are plotted for the noiseless, noisy and estimated geodesic quaternions for one of the simulations at $\sigma = \pi/16$ in Figure 14. These results give confidence in the proposed quaternion-based method.

APPENDIX D

This appendix illustrates that the distance metric for solving for the direction of best-fit geodesic to a set of quaternions is bi-invariant (*i.e.*, independent of the choice of coordinate system). For an arbitrary quaternion, a , left invariance is illustrated by left multiplying all of the quaternions by a and showing that the distance is the same as without a . The initial guess for the direction is given by

$$\begin{aligned}\vec{v} &= \log((aq_m)^* a q_N) \\ &= \log(q_m^* a^* a q_N) \\ &= \log(q_m^* q_N)\end{aligned}\quad (31)$$

which is the same as in eqn (18). Similarly, the quaternions mapped to the tangent space at q_m are

$$\begin{aligned}\vec{p}_i &= \log(q_m^* a^* a q_i) \\ &= \log(q_m^* q_N)\end{aligned}\quad (32)$$

As both \vec{v} and \vec{p}_i are the same, d_i^2 as defined in (20) must also be the same.

Demonstrating right invariance is more involved. The initial guess for the direction is now given by

$$\begin{aligned}\vec{v} &= \log((q_m a)^* q_N a) \\ &= \log(a^* q_m^* q_N a)\end{aligned}\quad (33)$$

and the tangent points by

$$\vec{p}_i = \log(a^* q_m^* q_i a) \quad (34)$$

Note that inside the logarithm, the composition of q_m^* and q_i is undergoing rotation by a^* . Because the magnitude of the angle described $q_m^* q_i$ is unaffected by rotation, only the direction of the rotation axis changes, so we can write

$$\log(a^* q_m^* q_i a) = a^* \log(q_m^* q_i) a \quad (35)$$

Now the distance metric becomes

$$d_i^2 = \frac{\| (a^* \log(q_m^* q_N) a) \times (a^* \log(q_m^* q_i) a) \|^2}{\| a^* \log(q_m^* q_N) a \|^2} \quad (36)$$

Recall that for two vectors, \vec{x} and \vec{y} , their cross-product is

$$\vec{x} \times \vec{y} = \|\vec{x}\| \|\vec{y}\| \sin(\theta) \vec{n} \quad (37)$$

Because the lengths of the vectors and the angle between them are unaffected by rotation, applying a rotation with matrix R to the two vectors results in the cross-product

$$\begin{aligned}(R\vec{x}) \times (R\vec{y}) &= \|\vec{x}\| \|\vec{y}\| \sin(\theta) R\vec{n} \\ &= R(\vec{x} \times \vec{y})\end{aligned}\quad (38)$$

Therefore, (36) can be rewritten as

$$\begin{aligned}d_i^2 &= \frac{\| a^* (\log(q_m^* q_N) \times \log(q_m^* q_i)) a \|^2}{\| a^* \log(q_m^* q_N) a \|^2} \\ &= \frac{\| \log(q_m^* q_N) \times \log(q_m^* q_i) \|^2}{\| \log(q_m^* q_N) \|^2}\end{aligned}\quad (39)$$

as desired.